Four Earthquakes of the Sumatran Fault Zone (Mw 6.0-6.4): Source Parameters and Identification of the Activated Fault Planes

Madlazim[1]* and B.J. Santosa[2]

1. Doctoral Candidate, Physics Department, Faculty of Mathematics and Science, ITS Jl. Arif Rahman Hakim I, Surabaya 60111, Indonesia,
* Corresponding Author; email: m_lazim@physics.its.ac.id
2. Professor, Physics Department, Faculty of Mathematics and Science, ITS Jl. Arif Rahman Hakim I, Surabaya 60111, Indonesia

ABSTRACT

Four earthquakes (Mw 6.0-6.4) which occurred at 3 major segments of Sumatran Fault Zone (SFZ) were analyzed to identify their fault planes. The events were relocated to assess physical insight into the hypocenter uncertainty. The earthquake source parameters were determined from three-component local waveforms recorded by IRIS-DMC and Geofon broadband IA networks. The epicentral distances of all stations were less than 10°. Moment tensor solutions of the events was performed, simultaneously with the determination of the centroid position. Joint analysis of the hypocenter position, centroid position and nodal planes of the events indicated the Sumatra fault planes. The hypocenters of all four events clearly prefer that strikes parallel to Sumatra Island to be the fault plane in all cases. Regional moment tensor solutions of this paper along with the focal mechanisms, which represent the only double couple of moment tensor, is plotted. The MT solutions consist of all events have strike slip one fault type. The preferable seismotectonic interpretation is that the events activated Sumatra fault zone at a depth of about 14-18 km, corresponding to the interplate of Sumatra fault boundary.

Keywords:
Sumatran fault zone;
3-component local
waveform inversion;
Source parameters and
fault plane

1. Introduction

Four earthquakes (M_w 6.0-6.4) which occurred at Sumatran Fault Zone (*SFZ*), have been recorded and reported by *IRIS-DMC* and *IA* local stations and can be accessed at http://www.iris.edu/dms/wilber.htm and http://geofon.gfz-potsdam.de/geofon/new/netabs/ia_req.html. The selected events occurred at 10 segments of *SFZ* during the period from December 1, 2007 to October 1, 2009. The Sumatra Fault Zone (*SFZ*) accommodates most of the right-lateral strain from slab relative movement and has been suggested as an active zone since Mid-Miocene [1]. West Sumatra is the boundary of ocean slab consisting of two faulting systems, which are strike-slip faulting system that rotate toward right direction (sinitral) and interface dip-slip subduction which has bigger influence [2].

The *SFZ* passes through the entire island. The fault is divided into three segments, namely, south-ern, central and northern segments. The fault is thrust type with a dextral sense. *SFZ* probably dates from the Middle Miocene and the opening of the Andaman Sea, although the relative motions of the major plates have changed little since the Middle Eocene [2]. The *SFZ* runs the length of the Barisan Mountains, a range of uplifted basement blocks, granitic intrusions, and Tertiary sediments, topped by Tertiary-Recent volcanics. Studies of Mesozoic outcrops in central Sumatra suggest that the *SFZ* has a displacement of approximately 150*km* in this area. It is however noted that strike slip deformation is distributed over a geographically wide area outside the present active trace of the *SFZ*.

Sieh and Natawidjaya [2] divided the Sumatran fault into 19 segments as demonstrated in Figure (1) and Table (1). The nomenclatural inherited from numerous earlier studies includes many fault names
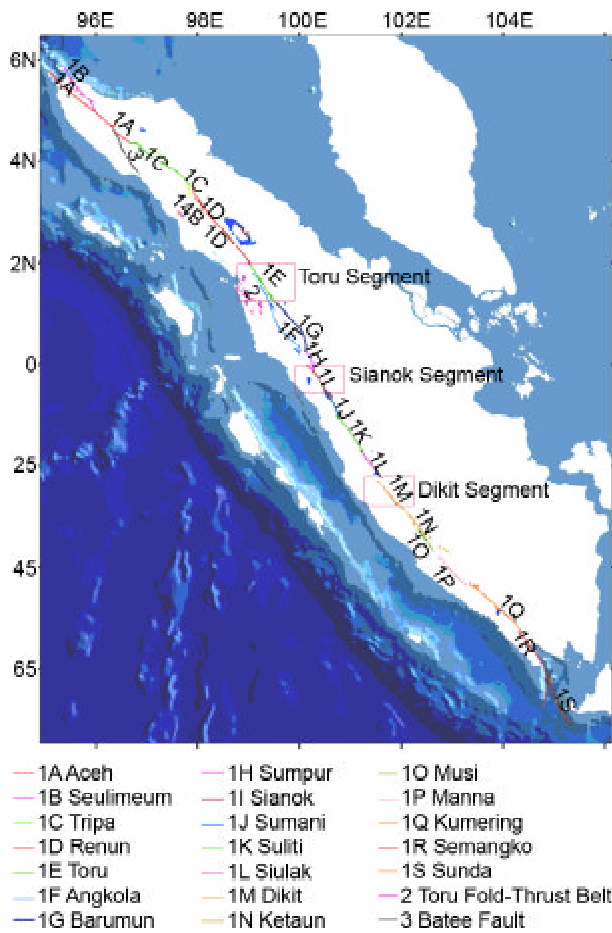
Figure 1. Modified map of geometrically defined of 19 segments of SFZ from [4] and the 3 segments of interest in this research (rectangles).

derived from nearby cities, districts, basins, and rivers. This is the most detailed article about characterization of *SFZ* segments, however, they have not considered seismic moment tensors and identification of fault planes of each *SFZ* segments.

Three components waveform inversion analysis of local data that was recorded by *IRIS-DMC* and Geofon *IA* were used in this study. The networks have been installed around *SFZ*. The purpose of this study is to locate the earthquakes, analyze their focal mechanisms and identify fault planes in this poorly study area. It is based on combination of the hypocentre relocations and moment tensor solutions, both with an emphasis on the uncertainty estimation. For the 4 events the moment tensors solution can also include calculation of the centroid position. Then the fault plane is one of the nodal planes passing through the centroid, the one which contains the hypocenter. For large events, the hypocenter and centroid do not coincide with each other. For smaller events ($M_w < 4$), for which the centroid and hypocenter are closer to each other, the moment tensors is calculated just for the hypocentre position. In this paper, the relation of such moment tensors solutions with the possible fault plane suggested by the 4 events is investigated.

Table 1. Sumatran Fault Zone Major Segments.

No.	Segment	Latitude	Length (km)	Large Historical Earthquakes
1	Sunda	6.75°S -5.9°S	~150	No Record
2	Semangko	-5.9°S -	65	1908
3	Kumering	5.3°S -4.35°S	150	1933 (M_s = 7.5), 1994 (M_W = 7.4)
4	Manna	4.35°S -3.8°S	85	1893
5	Musi	3.65°S-3.25°S	70	1979 (M_s = 6.6)
6	Ketaun	3.35°S -2.75°S	85	1943 (M_s = 7.3), 1952 (M_s = 6.8)
7	**Dikit**	**2.75°S -2.3°S**	**60**	No record
8	Siulak	2.25°S -1.7°S	70	1909 (M_s = 7.6), 1995 (M_W = 7.0)
9	Suliti	1.75°S -1.0°S	95	1943 (M_s = 7.4)
10	Sumani	1.0°S -0.5 °S	60	1943 (M_s = 7.6), 1926 (M_s~7)
11	**Sianok**	**0.7°S -0.1°N**	**90**	1822, 1926 (M_s~7)
12	Sumpur	0° -0.3°N	35	No Record
13	Barumun	0.3°N -1.2°N	125	No Record
14	Angkola	0.3°N -1.8°N	160	1892 (M_s = 7.7)
15	**Toru**	**1.2°N -2.0°N**	**95**	1984 (M_s = 6.4), 1987 (M_s = 6.6)
16	Renun	2.0°N -3.5°N	220	1916, 1921 (m_b = 6.8), 1936 (M_s=7.2)
17	Tripa	3.4°N -4.4°N	180	1990 (M_s = 6?), 1994 (M_W = 6?)
18	Aceh	4.4°N -5.4°N	200	No Record
19	Seulemeum	5.0°N -5.9°N 120	120	1964 (M_s = 6.4)

The segments of interest in this research are in bold.

2. Tectonic Context

West Sumatra is the boundary of ocean slab consisting of two faulting systems, which are strike-slip faulting system that rotate toward right direction (sinitral) and interface dip-slip subduction which has bigger influence. The basic kinematic role of the Sumatran Fault Zone (*SFZ*) is rather simple: It accommodates a significant amount of the strike-slip component of the obloque convergence between the Australian/Indian and Eurasian plates [2]. The Sumatra fault zone has a class of trench-parallel strike-slip fault system that works in concert with subduction zones to accommodate obliquely convergent plate motion [3].

Superimposed upon the broad sinusoidal geometry of the *SFZ* are more than a dozen discontinuities, see Figure (1) [4], ranging in width from ~5 to 12*km*. Major local changes in strike also occur. Most of the discontinuities are right steps in the fault trace and thus represent dilatational step overs, however, a few contractional bends also occur. Theoretically, these discontinuities and bends in the fault are large enough to influence the seismic behavior of the *SFZ* [2].

Crustal deformation rates (1900-2000) estimated for the Sumatra arc region highlight (i) large variations in dextral shear motion (seismic slip) from 1*mm/yr* to 29*mm/yr* along the Sumatran Fault Zone (*SFZ*), (ii) dominantly compression with deformation velocities as high as 19 mm/yr near the equator along offshore Sumatra fore-arc [5]. Combined analysis of historical triangulation and recent *GPS* measurements along the *SFZ* indicate slip rates of 23 to 24*mm/yr* [6]. There is a general northward increase in slip rate along the *SFZ* [7-8].

3. Method

3.1. Three Components Local Waveform

The three components local waveform recorded by *GEOFON* broadband *IA* and *IRIS-DMC* net-

works were used in this study. The epicentral distances of the eleven stations were less than 10°, see Figure (2).

3.2. One D Velocity Model for This Area Study

Four 1*D* velocity models were verified for this area study to calculate moment tensors. Variance reduction and *DC*-percentage, as a result of the moment tensors calculation using modified *H-S*, see Table (2), *H* [9], *H-S*, see Table (3) [10], and *T* crustal model [11], were compared. The moment tensors solutions using the *H-S* crustal model, see Table (4), produced the largest variance reduction and the *DC*% as presented later in the paper in Table (6). Therefore, the *H-S* model, see Table (4) was used to further calculate the moment tensors.
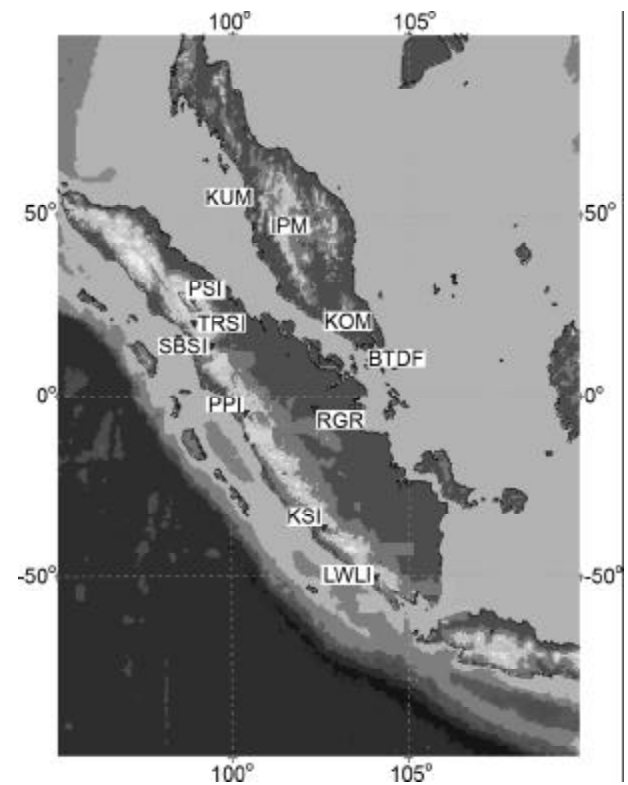

Figure 2. Map of the stations recorded local waveforms which was used for the MT calculation.

Table 2. The 4 events as located in this study by HYPOINVERSE and from IRIS-DMC and GEOFON.

Agency	Date	Origin	HYPOINVERSE								IRIS-DMC/GEOFON		
			Latitude (deg.)	Longitude (deg.)	Depth (km)	No. P&S	RMS	ERH	ERZ	M_w	Latitude (degr.)	Longitude (degr.)	Depth (km)
Geofon	20070306	0349270	-0.53	100.51	10	20	0.61	2.1	2.0	6.2	-0.44	100.45	10
Geofon	20070306	05:49:26	-0.55	100.50	14	20	0.74	2.3	1.8	6.1	-0.44	100.41	10
IRIS	20080519	14:26:45	1.50	99.18	18	20	0.65	1.2	1.9	6.0	1.64	99.15	10
Geofon	20091001	01:52:34	-2.61	101.56	16	24	0.58	1.5	1.6	6.4	-2.5	101.5	9.7

Table 3. Three crustal models with homogeneous layers used inversion for the location.

Modified H-S		H		T	
Vp (km/s)	Depth (km)	Vp (km/s)	Depth (km)	Vp (km/s)	Depth (km)
2.31	0.0	3.50	0	5.70	0
5.52	2.0	5.47	0.5	6.00	5
6.41	16.0	5.50	2	6.40	18
6.70	33.0	6.00	5	7.90	39
		6.20	10		
		6.48	15		
		6.70	20		
		6.75	30		
		8.00	40		

Table 4. H-S velocity model for full waveform.

Vp (km/s)	Depth (km)	Vs (km/s)	Rho (g/cm**3)	Qp	Qs
2.31	0.0	1.300	2.500	300	150
4.27	1.0	2.400	2.900	300	150
5.52	2.0	3.100	3.000	300	150
6.23	5.0	3.500	3.300	300	150
6.41	16.0	3.600	3.400	300	150
6.70	33.0	4.700	3.400	300	150
8.00	40.0	4.760	3.500	1000	500

The Vp/Vs = 1.76 was adopted for three the models.

3.3. Hypocentral Locations

Hypocentral locations were improved by using *HYPOINVERSE* code [12]. This study focuses on 4 events, listed in Table (2). The location was performed using 20-24 stations from the *IRIS-DMC* and *GFZ-Potsdam* (Geofon) networks. Only manual picks of *P* and *S*-wave arrival times were made and processed with the derived *H-S* crustal model as presented in Table (2). This crustal model was modified from *H-S* crustal model, see Table (4). It was done by trial, tested and adjusted using standard criteria: The *H-S* crustal model in Table (3) is combination of Haslinger et al [9] and Santosa [10] crustal model. Hypocenters were located using *HYPOINVERSE* code [12]. *RMS* (root mean square residual), *ERH* (horizontal error) and *ERZ* (vertical error) [13] are provided by the same code. The model that exhibited the smallest errors was chosen.

Several tests were carried out in order to use the most appropriate 1*D* model and identified the parameters that would lead to the most stable results [13]. Four 1*D* crustal models, see Tables (3) and (4), were employed: modified *H-S* with its number of layer modified to have 4 layers with $V_p/V_s = 1.76$ *km/s*. *H*,

T and *H-S* models, see Table (3), are taken from [9-11] respectively. The criteria for choosing the most suitable crustal model were the standard *RMS*, *ERH*, *ERZ* errors. In the beginning the whole 4-events dataset was used; setting the ratio $V_p/V_s = 1.76$ and the trial ("starting") depth to 18*km*, the 4 models were tested. The errors showed that the preferable model (leading to the smallest error) is modified *H-S* model. The modified *H-S* model corresponding locations are listed in Table (4). Another reason to prefer the *H-S* model comes from the stability test in terms of the trial source depth in *HYPOINVERSE* code. We varied the trial depth (10, 14, 18… *km*) and observed its effect upon the location depth.

The *H-S* model, produced better stable results than *H* and *T* models, see Table (4). But the results of the stability are worse than those modified *H-S*, as shown in Table (3), due to the large number of layers in the *H-S* model. The *T* model produced the least stable results, due to the large number of layers in that model and relatively large velocities in the top most layers. The instability is related to head waves from intra-crustal discontinuities. On the contrary, modified *H-S*, with its low number of layers and relatively low velocities at its top, is the most stable. The *H* model is an intermediate case. The stability test like this is important for preventing the unstable solutions. However, it can not be used for optimizing the depth estimate [13]. By, varying the trial depth, not only the resulting hypocenter depth varies, but also the resulting epicenter is shifted. The horizontal and vertical positions move in such a way that the *RMS* misfit stays constant; hence none of the depths can be preferred. The next tests were performed for the 4 events. The values of the ratio V_p/V_s were varied (1.74, 1.75, 1.76,1,77,….1.79). The results showed that the modified *H-S* model was still the most appropriate. Additionally, the modified *H-S* model with the V_p/V_s ratio value of 1.76 was the optimum combination.

In order to improve the depth estimate of the events, the following method was used. For each event, its *HYPOINVERSE* epicenter was kept fixed, and the depth was found by grid-search minimization of the travel-time residual. This useful trick aims at overcoming the unfavorable fact that the time residuals are affected by the depth variation much less than by the epicenter variation [13]. If retriev-

ing both the depth and the horizontal position, the depth resolution is low. That is why the depth was decoupled by fixing the epicenter. Moreover, the grid search is free from limitations of the linearization used in *HYPOINVERSE* code [12]. The corresponding hypocenters are listed in Table (2).

3.4. Data Processing

Waveforms analyzed in this study were initially taken from eleven regional broad band stations. The first-motion polarities were read from all broad band records, paying close attention to the consistency of the three components to avoid erroneous orientation of the sensor and/or problematic azimuths [14].

The waveforms were processed by using the Seismic Analysis Code (*SAC*) software, the instrumental correction was first performed on the selected seismograms [15-16]. Before moment tensors inversion, the velocity records are integrated once, and the acceleration records are integrated twice, in the frequency band of 0.01-$0.07 Hz$. Complete three-component waveforms are employed without separation of specific wave groups; these were re-sampled at all stations into 9567 points, with a time step of $0.04 sec$. Waveforms are not shifted to artificially match the first arrival time. The reason is obvious: if the misfit comes from inaccurate location or a local structure at the station, then a simple shift of the whole waveform is not the appropriate correction. The only case where such a shift might be acceptable is when the station had grossly wrong timing, that is, by a few seconds. Such a situation can be detected by checking the location P residuals at all stations used for the moment tensors calculation, where it is a simple check but is often overlooked in practice. No failure like this was detected in this article.

The instrumental correction and further processing was performed with *ISOLA* software [16]. *ISOLA* software starts from band-passes velocity traces, converts them to displacement and inverts full waveforms into moment tensors.

3.5. Moment Tensors Calculations Using ISOLA Software

Moment tensors of four events were calculated by waveform inversion of three-component broad-band records of *IRIS-DMC* and *GEOFON-IA*. The networks belong to the Incorporated Research Institutions for Seismology and *GFZ* German Research Centre for Geosciences, respectively. More details and present status of the networks and their stations can be found at the their websites.

Moment tensor calculation of this study was conducted using 1-*D* crustal velocity model [9-10], the stations, see Figure (2), and frequency range of 0.015-$0.09 Hz$ varying for each event. The different filters mean different signal-to-noise ratio related to smaller magnitudes and different location and depths. The low frequency is preferred because in this case the modeling is less dependent (inherently) on earth crust structure.

The *ISOLA* software was used, combining the computational speed of Fortran and the users' comfort of Matlab [16]. It makes use of the inverse-problem formulation [17] based on six elementary MTs. Their equation is used to quickly evaluate the correlation between observed and synthetic waveforms. The Green's functions are calculated using the discrete-wavenumber method [18-19]. The match between the observed and best-fitting synthetic data is characterized by the overall variance reduction = 1-E/O, where $E = \Sigma (O_i - S_i)^2$, $O = \Sigma (O_i)^2$, with O and S standing for the observed and synthetic data, along with summation over all samples, components, and stations. The code also allows for complex rupture histories described by multiple point-source subevents, each one represented by a delta function [20].

The three components waveform inversion was conducted using iterative deconvolution method [20]. This method was implemented for regional distances in the *ISOLA* software [16]. Complete waveforms were used without any separation of the body waves and surface waves. Waveform data processing is very easy to do, because it uses Fortran_Matlab *ISOLA_GUI* package program [16]. The code gives an opportunity to use multi source-point model. In this study, we focused on using single source and deviatorical inversion (without any volume changes). Deviatorical tensor decomposition commonly consist of two components, which are double-couple (*DC*) part and compensated linear vector dipole (*CLVD*) part, as a (non-*DC*) component. In this study, both components were determined. But, the benefit of non-*DC* component as a physical parameter of tectonic earthquake is very limited, because the available crustal model is only an approximation.

The moment tensors calculations need an estimate of the source position. Here we distinguish between hypocenter and centroid. Centroid represents the center of gravity of the faulted area. The centroid can be determined during the moment tensors retrieval as a point optimizing the waveform fit, found by grid search around an assumed position. Analogously, a temporal grid search provides the centroid time. For large events, the hypocenter and centroid do not coincide with each other.

The moment tensors calculations for the four events were done using optimum source positions and time grid-search in three stages by *ISOLA* software [16]. First, we start with a 25-36 point grid stencil centred below the *IRIS-DMC* or *GEOFON* epicentres and depths 10, 20, 35,… 45*km*, with 10-20*km* increments both in the *NS* direction and *EW* direction. For each event, three such stencils are placed at the depths of 11, 30 and 60*km*. At each depth, the moment tensor corresponding to the optimum time is highly variable with the trial spatial positions, where the correlation has its maximum value. Secondly, the moment tensors were computed along a vertical line passing through the optimum position from the previous stage. Third, fixing the optimum depth of the optimum position, we focused on the spatial-temporal search. The moment tensors calculations for all events use the hypocenters by *HYPOINVERSE* code, see Table (2). Figures (3a) to (3d) show the waveforms fit for the moment tensor
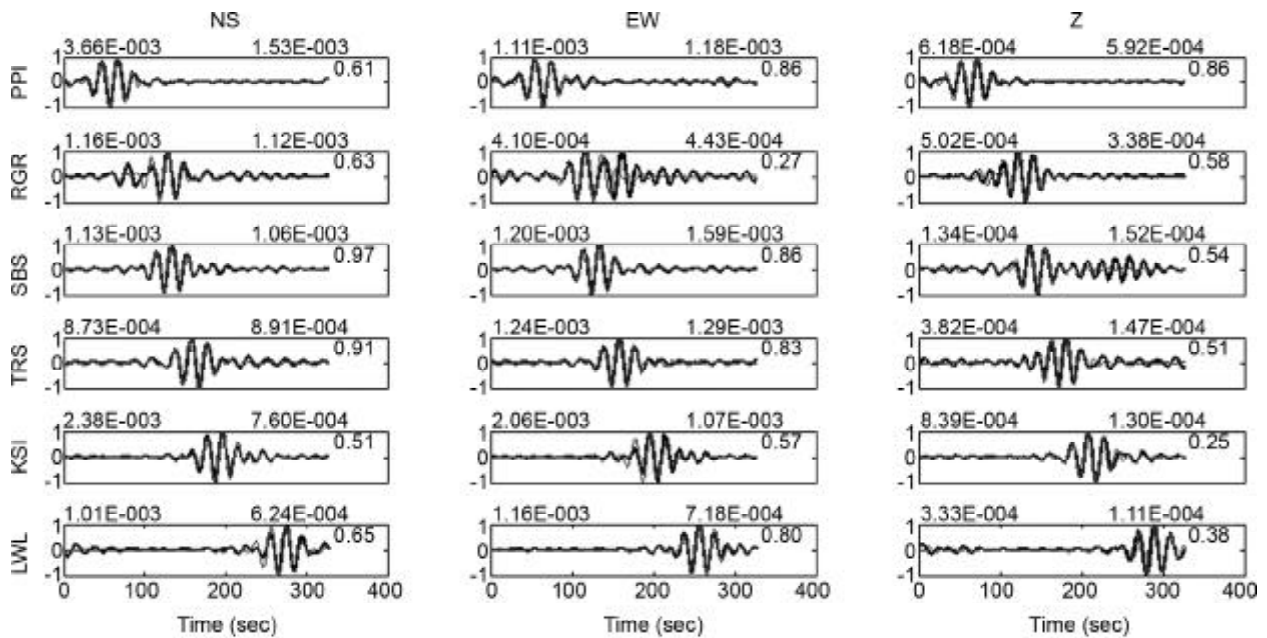
a) Waveforms of 20070306_03:49:40 Event
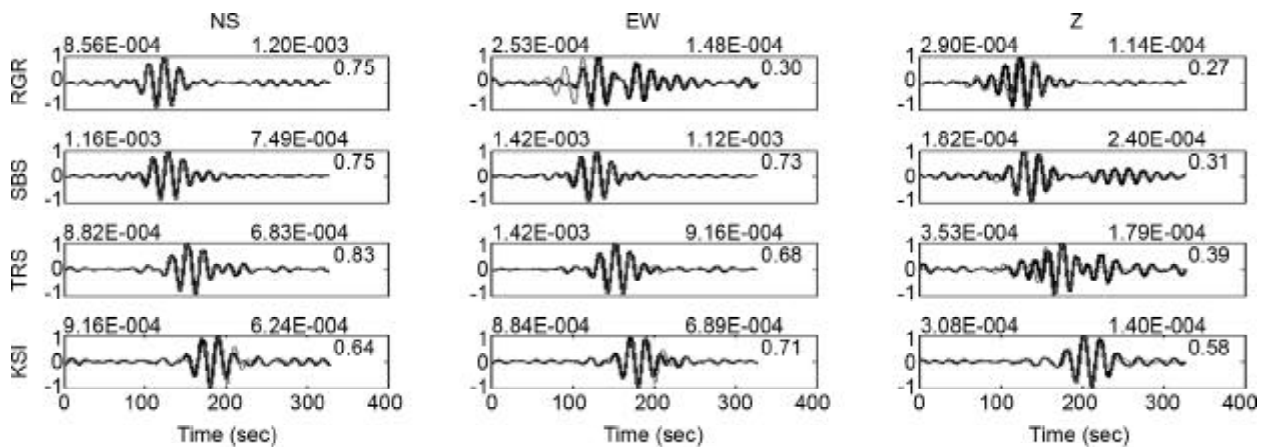
b) Waveforms of 20070306_05:49:26 Event

Figure 3. The waveforms fit for a moment tensor solution; grey waveforms are the synthetic, black waveforms are the observed and black numbers are variance reductions.
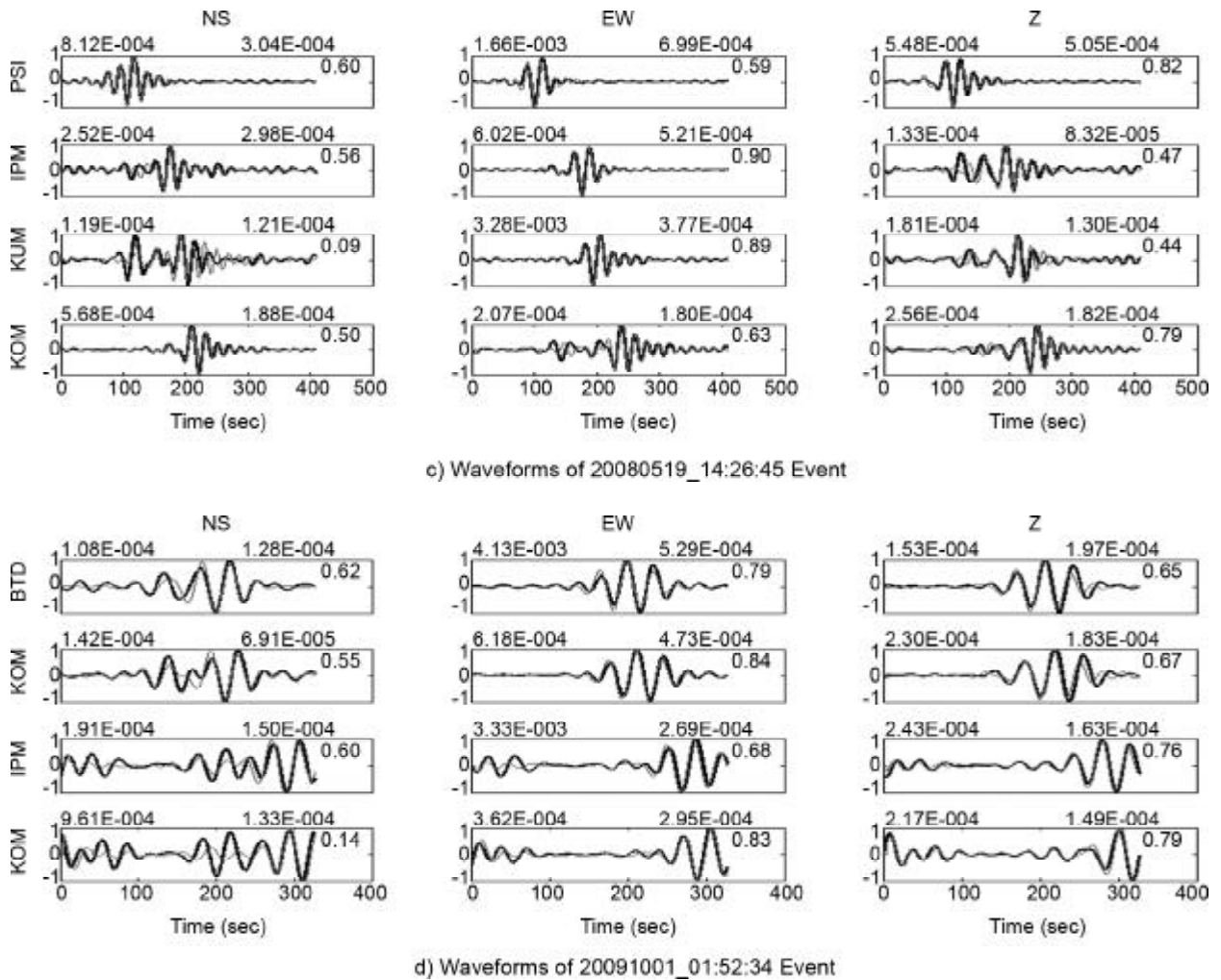
c) Waveforms of 20080519_14:26:45 Event

d) Waveforms of 20091001_01:52:34 Event

Figure 3. Continued...

solutions for *NS* (North-South), *EW* (East-West) and *Z* (vertical) components of 20070306_03:49:40, 20070306_05:49:26, 20080519_14:26:45 and 20091001_01:52:34 events, respectively. Grey waveforms are the synthetic, black waveforms are the observed and black numbers are variance reductions.

3.6. Fault Plane Identifications

The fault planes were identified of the four events using *H-C* method [13, 21]. All events were also checked for the mutual position of the hypocenter and centroid, *H* and *C*. The centroid (*C*) was determined by repeated calculations of the moment tensor in a volume grid of trial source positions not far from the hypocenter, aiming at optimizing the fit between the observed and synthetic waveforms. This so-called hierarchic grid search was applied [13, 20], using a progressively finer grid while approaching towards the likely centroid position. The optimum source positions (*C*) were identified at the

locations shown in Table (5). Due to the low-frequency nature of the *MT* waveform inversion, the centroid position cannot be resolved better than with the inaccuracy of a few kilometers [13, 21].

Earthquake source parameters were used to identify the orientation of event's fault plane. To identify the true fault plane orientation, *H* (Hypocenter) -*C* (Centroid) method was used [13, 21]. Combined knowledge of *C*, the *MT* solution (nodal planes) and hypocenter position *H* is the key to identify the fault plane. The nodal planes pass through *C*, and the fault plane is that one comprising *H*. Although the idea is simple, its successful application needs a great caution in the determination of *H* and *C*, and therefore, it is hardly applicable at a routine processing level [13].

If hypocenter, centroid and nodal planes are consistent, comparison between mutual position of the hypocenter with the centroid and the two nodal planes passing through the centroid for event

demonstrate that the hypocenter is near to nodal planes, enabling identification of any nodal plane as the fault plane. The procedure with the location and *MT* data of this paper, see Tables (4) and (5), was shown by Figures (4a) to (4d). The hypocenters of all 4 events clearly prefer strikes parallel to Sumatra Island, thus indicating that nodal plane to be the fault plane. Distances *H* to nodal planes and to *C* are demonstrated in Table (6).

4. Results

Four events of the March 6, 2007 to October 1, 2009 were located with *HYPOINVERSE*, using manual measurements from Geofon-*IA* and *IRIS-*

Table 5. Focal mechanism obtained by the MT inversion.

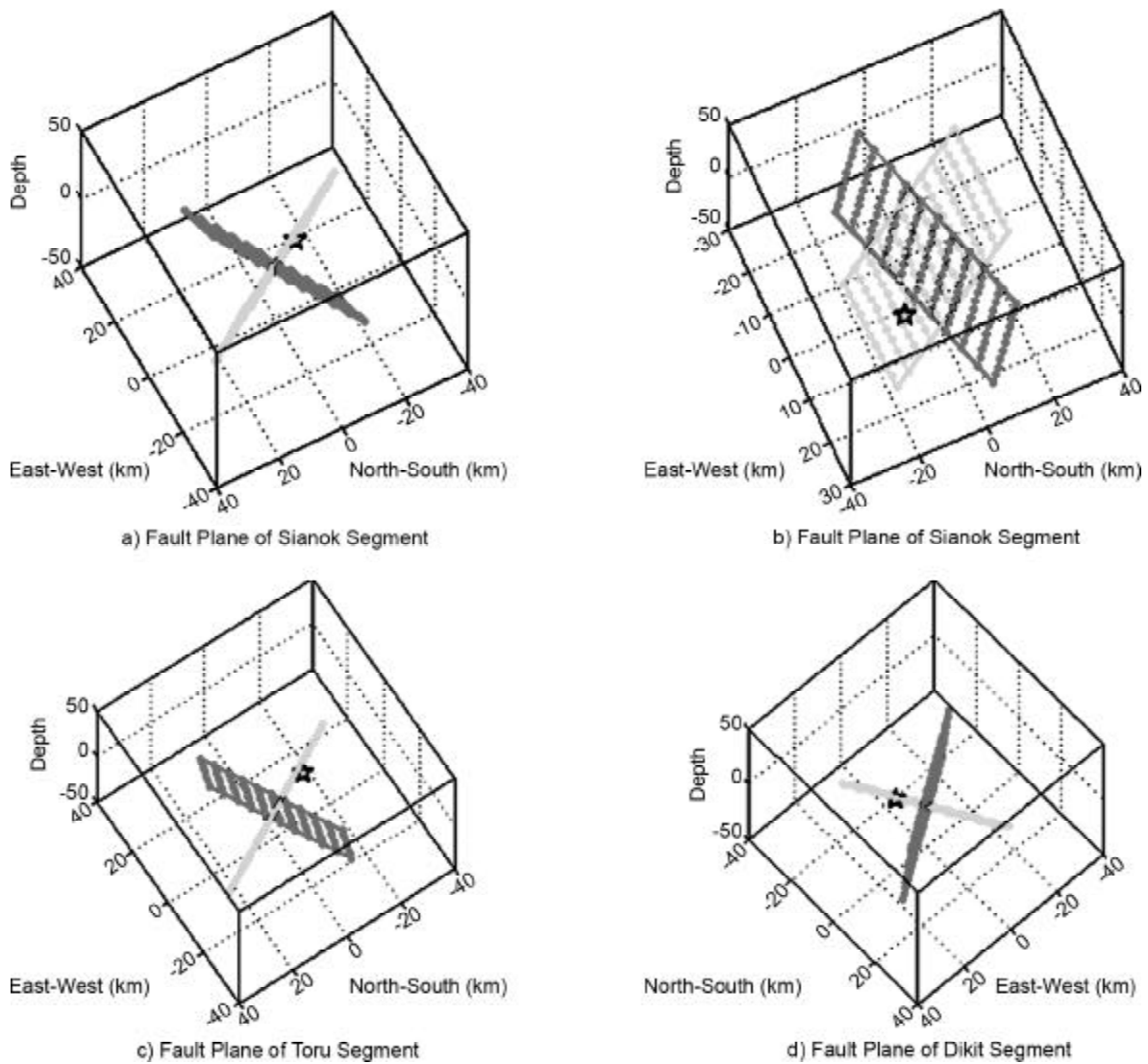| Event#	M_w	Strike (deg.)	Dip (deg.)	Rake (deg.)	Number of Stations	Centroid			DC%	Variance Reduction%
						Lat. (deg)	Long. (deg)	Depth (km)		
20070306_03:49:40	6.2	328	79	163	6	-0.45	100.47	12	85.8	64
20070306_05:49:26	6.1	335	71	168	4	-0.47	100.42	12	96.6	76
20080519_14:26:45	6.0	154	79	-176	4	1.63	99.15	20	95.1	71
20091001_01:52:34	6.4	149	68	-176	4	-2.54	101.55	12	92.4	73

Figure 4. Fault plane identification of 4 events that occurred at 3 segments of SFZ, see Table (6). Two nodal planes pass through the centroid (LAT=0 and LON=0), both according to the MT solution of this paper, and the hypocenters for all events. These are the favorable cases, with hypocenter in one of the nodal planes, thus indicating the fault plane.

a) Fault Plane of Sianok Segment b) Fault Plane of Sianok Segment c) Fault Plane of Toru Segment d) Fault Plane of Dikit Segment

Table 6. Criteria used for the identification of the fault planes for each studied event.

Event	Segment	Distance of H2G (km)	Distance of H2R (km)	Distance of H2C (km)	Fault Plane Strike (deg)	Fault Plane Dip (deg)
20070306_03:49:40	Sianok	2.73	9.76	9.75	328	79
20070306_05:49:26	Sianok	3.25	13.19	14.47	335	71
20080519_14:26:45	Toru	2.53	14.14	14.38	154	79
20091001_01:52:34	Dikit	1.30	9.87	10.58	149	48

H2G:distance H to grey plane; H2R:distance H to black plane; H2C:distance H to C

DMC permanent networks. We tested four 1*D* models and selected the one with the best fit (minimum errors); the model is referred to as modified *H-S* model. Stabilization tests were also performed for the four events (M_w 6.0-6.4).

In the next step, moment tensors of the four events were calculated by waveform inversion of three-component broadband records of Geofon-*IA* and *IRIS-DMC* networks. The moment tensors (*MT*) inversion of regional waveforms was performed by the least square method. The centroid, see Table (6), was determined by repeated calculations of the *MT* in a volume grid of trial source positions not far from the hypocenter, aiming at optimizing the fit between the observed and synthetic waveforms.

Finally, the fault plane for the events was identified. Results of the identification are presented in Table (5) and Figure (4).

5. Discussion

The Great Sumatran fault carries most of the strike-slip component of oblique convergence across the Sumatran plate boundary. These information can be accessed at (http://www.tectonics.caltech.edu/sumatra/sumatranfault.html). Figure (5) is the main result of the whole paper, where 4 events have strike slip fault type.

The two events that occurred on the Sianok segment have strike slip fault types, see Figure (4). Here the shallow events (10 and 14*km*) are located, as shown in Figure (5), with centroid locations 12*km*, see Table (6), and also characterized by a consistent strike-slip component. Geomorphic expression of the fault is particularly interesting along the Sianok segment because it traverses the flank of Marapi volcano and the young, 200-*m*-thick pyroclastic flow deposit of Maninjou volcano [2]. In this study, the two events were analyzed at this segment, mainshock and one aftershock, see Table (6). The Sianok segment is predominantly straight and continuous
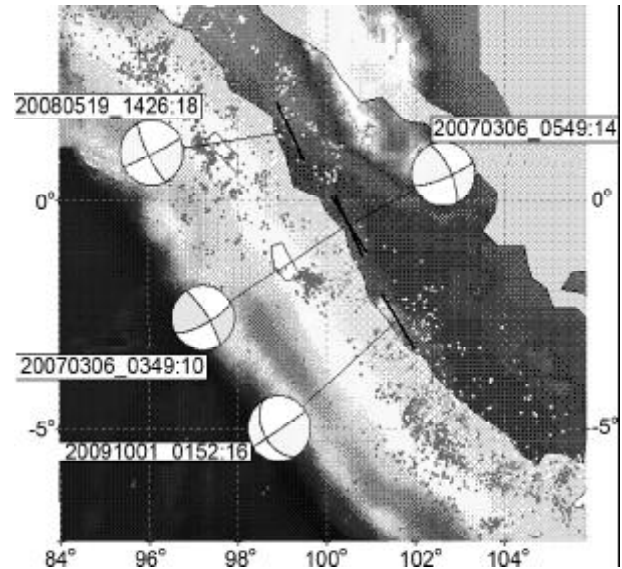

Figure 5. CMTs with epicenters, (event (yyyymmdd_hhmm): depth (km)) in white rectangles, (grey beachball parts and white beachball parts)), strike line (black line) and fault type.

segment runs ~90*km* from the northeast shore of Lake Singkarak, along the southwest flank of the great strato volcano Marapi to a 10-km-wide right step over at the Equator [2]. Its southern 18*km*, on the flank of Lake Singkarak, is accurate and must have a significant component of normal faulting down toward the lake.

The Toru segment has not produced a major historical earthquake, but right-lateral slip near the northern end of this segment did generate the $M=6.4$ Pahae Jahe earthquake of 1984. Northwest of Sibual-buali volcano, a 30-*km*-wide caldera northeast of the fault is truncated by the fault. The other half of the caldera (southwest of the fault) must be concealed beneath young volcanic deposits. The geomorphic expression of the fault in the vicinity of the truncated caldera is unusually complex. Significant components of dip slip occur on faults that splay northward from the main trace into the caldera [2]. In this study, we analyzed the event occurred on 20080519

at this segment. The event has strike, 154° and dip 79°, see Figure (4). Location and focal mechanism for the events suggest that these events occurred on Toru segment. Here the shallow (18*km*) events are located, as shown in Table (4).

Fault plane of the 20091001_01:52:34 event occurred at Dikit segment in this study has strike 149° and dip 48°, see Tables (5) and (6) and Figure (4). This event has strike slip fault type, see Figure (4). Here the shallow event (16*km*) is located as shown in Figure (6), with centroid location 12*km*, as shown in Table (6), and characterized also by a consistent strike-slip component. The fault plane of the event occurred has strike 149° and dip 68°, see Tables (5) and (6) and Figure (4). This event has strike slip fault type, see Figure (4). Sixty *km*-long Dikit segment with several short obscure sections along its northern few kilometers, see Figure (1). It shares a contractional step over with the Ketaun segment on its southeastern end. Its northwestern termination is at one of the larger dilatational step over along the Sumatran fault. On the southwestern flank of this 11-*km*-wide step over, the Dikit segment disappears into the edifice of the small strato volcano Kunyit. This is one of the few clear associations of a dilatational step over and a volcano along the Sumatran fault [2].

6. Conclusion

Regional moment tensor (*MT*) solutions are shown in Figure (5), along with the focal mechanisms, which represent the major double couple of the deviatoric *MT*. The *MT* solutions consist of all events which have strike slip one fault type. The event numbers labeled above each focal mechanism are coded in Table (6).

The hypocenters of all 4 events clearly prefer a high dip nodal to be the fault plane. Almost all focal mechanisms demonstrate the presence of one high dip nodal and most strike parallel with Sumatra Island. Since there is limited depth accuracy the definition of a single high dip nodal, along which the hypocenters are distributed comprises uncertainty. Therefore, the final interpretation is the approximation depth of about 14-18*km*. In this sense, our results support the hypothesis that the interplate boundary of the Sumatra fault zone plays a role of active surface.

References

1. McCarthy, A.J. and Elders, C.F. (1997). "Cenozoic Deformation in Sumatra: Oblique Subduction and the Development of the Sumatran Fault System", In: Fraser, A.J., Matthews, S.J., Murphy, R.W. (Eds.), Petroleum Geology of Southeast Asia, Special Publications, **126**, Geological Society, London, doi:10.1144/ GSL.SP.1997.126.01.21, 355-363.

2. Seih, K. and Natawidjaya, D. (2000). "Neo-tectonics of the Sumatra Fault, Indonesia", *Journal of Geophysical Research*, **105**, 295-326.

3. Yeats, R., Sieh, K., and Allen, C. (1997). "*The Geology of Earthquakes*", 568p., Oxford Univ., Press, New York.

4. Natawidjaya, D.H. (2007). "The Sumatran Fault Zone-from Source to Hazard", *Journal of Earthquake and Tsunami*, **1**, 21-47.

5. Lasitha, S., Radhakrishna, M., and Sanu, T.D. (2006). "Seismically Active Deformation in the Sumatra-Java Trench-Arc Region: Geodynamic Implications", *Current Science*, **90**(5), 690-696.

6. Prawirodirdjo, L., Bock, Y., McCaffrey, R., and et al (1997). "Geodetic Observations of Inter-seismic Strain Segmentation at the Sumatra Subduction Zone", Geophysical Research Letters, **24**, 2601-2604.

7. McCaffrey, R. (1991). "Slip Vectors and Stretching of the Sumatran Fore Arc", *Geology*, **19**, 881-884.

8. Bellier, O. and Sebrier, M. (1995). "Is the Slip Rate Variation on the Great Sumatran Fault Accommodated by Fore-Arc Stretching?" *Geophys. Res. Lett.*, **22**, 1969-1972.

9. Haslinger, F., Kissling, E., Ansorge, J., Hatzfeld, D., Papadimitriou, E., Karakostas, V., Makropoulos, K., Kahle, H.-G., and Peter, Y., (1999). "3D Crustal Structure from Local Earthquake Tomography Around the Gulf of Arta (Ionian Region, NW Greece)", *Tectonophysics*, **304**, 201-218.

10. Santosa, B.J. (2005). "Analyzing the Seismogram of Earthquakes on Sumatra-Java Subduction Plane at CHTO Observation Station", *Journal MIPA*, **13**, 23-29.

11. Tselentis, G.-A., Melis, N.S., Sokos, E., and Papatsimpa, K. (1996). "The Egion June 15, 1995 (6.2 ML) Earthquake, Western Greece", *Pure Appl. Geophysics*, **147**, 83-98.

12 Klein, F.W. (1985). "HYPOINVERSE, a Program for VAX and Pro-350 Computers to Solve Fore-Earthquake Locations and Magnitudes", U.S. Geological Survey Open-File Report, 85-515.

13. Serpetsidaki, A., Sokos, E., Tselentis, G.A., and Zahradnik, J. (2010). "Seismic Sequence Near Zakynthos Island, Greece, April 2006: Identification of the Activated Fault Plane", *Tectonophysics*, **480**, 23-32.

14. Mandal, P., Satyamurty, C., and Raju, I.P. (2009). Iterative De-Convolution of the Local Waveforms: Characterization of the Seismic Sources in Kachchh, India, *Tectonophysics,* **478**, 143-157.

15. Zahradnik, J., Jamsky, J., and Plicka, V. (2008). "Detailed Waveform Inversion for Moment Tensors of M~4 Events: Examples from the Corinth Gulf, Greece, Bull. Seism. Soc. Am., **98**, 2756-2771.

16. Sokos, E. and Zahradnk, J. (2008). "ISOLA a Fortran Code and a Matlab GUI to Perform Multiple-Point Source Inversion of Seismic Data", *Computers & Geosciences*, **34**, 967-977.

17. Kikuchi, M. and Kanamori, H. (1991). "Inversion of Complex Body Waves - III", Bull. Seism. Soc. Am., **81**, 2335-2350.

18. Bouchon, M. (2003). "A Review of the Discrete Wavenumber Method", *Pure Appl. Geophys*, **160**, 445-465.

19. Coutant, O. (1990). "Program of Numerical Simulation AXITRA, Laboratoire de Géophysique Interne et Tectonophysique Report", University of Joseph Fourier (in French).

20. Zahradnik, J., Serpetsidaki, A., Sokos, E., and Tselentis, G.A. (2005). "Iterative Deconvolution of Regional Waveforms and a Double-Event Interpretation of the Lefkada Earthquake, Greece", Bull. Seism. Soc. Am., **95**(1), 159-172.

21. Zahradnik, J., Gallovic, F., Sokos, E., Serpetsidaki, A., and Tselentis, G.A. (2008). "Quick Fault-Plane Identification by a Geometrical Method: Application to the Mw 6.2 Leonidio Earthquake, 6 January 2008, Greece", Seismological Research Letters, **79**, 653-662.